DE GRUYTER Nanotechnology Reviews 2021; 10: 318–329

Research Article

Nuru-Deen Jaji, Muhammad Bisyrul Hafi Othman*, Hooi Ling Lee*, Mohd Hazwan Hussin, and David Hui

One-pot solvothermal synthesis and characterization of highly stable nickel nanoparticles

https://doi.org/10.1515/ntrev-2021-0019
received March 2, 2021; accepted March 6, 2021

Abstract: High stable nickel nanoparticles (NiNPs) have been successfully synthesized from nickel chloride as the precursor through a simple one-pot solvothermal process. A systematic investigation of the reaction parameters, namely, effects of reaction temperature, pH of precursor solution, the concentration of reactants, and reaction time on the formation of NiNPs, was carried out to obtain the optimal values for the synthesis. The optimum reaction temperature, pH, $NiCl_2{\cdot}6H_2O$ concentration, and reaction time are 190°C, pH 9, 0.1 M, and 24 h. The characteristic peaks of NiNPs have been confirmed by the Fourier transformer infra-red and surface plasmon resonance, with the presence of –OH stretching bands at 3,593 and 603 cm^{-1} (interaction with Ni and NiO) and λ_{max} 265 nm, respectively. The X-ray diffraction and transmission electron microscope demonstrated the particle size of about 24 nm (by Scherrer) and 49 nm (Image-J), respectively, with the face center cubic phase. The synthesized NiNPs showed good stability, where the degradation of NiNPs was completed at 800°C with more than 97% residue as depicted by the thermogravimetry analysis. The synthesized NiNPs can be used as fillers to enhance the thermal, mechanical, and electrical properties of polymeric materials.

Keywords: nickel nanoparticles, one-pot synthesis, solvothermal synthesis, nanotechnology

1 Introduction

In the last decade, extensive research has been focused on nanoscience and nanotechnology. Nanotechnology has led to the development of tailored materials such as nanoparticles, nanocomposites, and nanotubes. The significance of these materials increased due to their potential application [1]. Nanomaterials have attracted extensive attention due to their small-scale size, surface effects, and quantum tunneling properties. The unique properties of nanomaterials make them superior compared to their bulk counterparts. Hence, nanomaterials have broader potential applications [2] as indicated in the following examples. Nanomaterials have generated extensive attention in the construction of green and smart nanostructures of two-dimensional flexible paper-like materials. These hybrid papers have great potential for applications in sensing, electronics, chemical filters, and energy devices [3]. Magnetic nanoparticles are being investigated for potential applications attributed to their unique magnetic properties. Currently, they are explored for therapeutic and diagnostic applications, including magnetically guided drug delivery, image-guided drug delivery, and in alternating magnetic field application [4]. The current applications of magnetic nanoparticles include electron-transfer processes. The reduction of bipyridine derivatives on nickel particles was achieved by the effect of the microwave without changing the reaction temperature due to electron transfer [5].

In recent years, nanomaterial technology is emerging in diverse engineering fields such as the applications of

---

*** Corresponding author: Muhammad Bisyrul Hafi Othman,** School of Chemical Sciences, Universiti Sains Malaysia, 11800 Penang, Malaysia, e-mail: bisyrul@usm.my, tel: +604-6534032, fax: +604-6574854
*** Corresponding author: Hooi Ling Lee,** Nanomaterials Research Group, School of Chemical Sciences, Universiti Sains Malaysia, 11800 Penang, Malaysia, e-mail: hllee@usm.my, tel: +604-6533547, fax: +604-6574854
Nuru-Deen Jaji: School of Chemical Sciences, Universiti Sains Malaysia, 11800 Penang, Malaysia; Federal College of Education Technical, PMB 060, Gombe, Gombe State, Nigeria
Mohd Hazwan Hussin: School of Chemical Sciences, Universiti Sains Malaysia, 11800 Penang, Malaysia
David Hui: Department of Mechanical Engineering, University of New Orleans, New Orleans 70148, LA, United States of America

nanomaterials in ultra-high concrete with excellent toughness, high tensile strength, and high resistance to cracking [6], applications of magnetic Fe_3O_4 nanomaterials in magnetic resonance imaging for high penetration-depth, high sensitivity, and accurate tissue resolution in clinical imaging [7], polymer nanocomposite sunlight spectrum down-converters made by open pulsed laser deposition [8], materials advancement in the technological development for 5G wireless communications [9], and nanomaterial applications in the construction of biologically inspired physico-antimicrobial surfaces that will kill microbes landing on such surfaces [10].

Among the magnetic nanoparticles, nickel nanoparticles (NiNPs) have been widely studied for their nanoscale properties and applications in various fields. This includes its use in supercapacitors with high specific capacitance [11], where the NiNPs are deposited on nickel foams. The electrocatalytic activity of NiNPs was used in the oxidation of methanol and water. In this reaction, nickel phosphate nanoparticles showed high catalytic activity compared to platinum counter electrodes [12]. Supercapacitors have been fabricated from diverse materials depending on the type of energy storage and the capacitance required. Small bimetallic $CoNiS_x$ nanocrystallites embedded in N-doped carbon were grown on graphene oxide. Due to synergistic effects by the multiple structural morphology and composition, the nanocrystallites displayed significantly enhanced electrochemical performance as an advanced electrode material for supercapacitors. Nickel oxide nanomaterials are used as supercapacitors in energy storage [13]. Nickel selenide nanoparticles are used as a cheap alternative for the platinum counter electrode in dye-sensitized solar cells. The nickel selenide nanocrystals exhibited electrochemical activity in reducing triiodide to iodide and are therefore employed as the counter electrode in solar cells [14]. Nickel oxide nanoparticles serve as new hardware for neuromorphic computing. The electrospun nanofiber of nickel oxide enables data storage as well as data transfer in neuromorphic computing [15]. In catalytic applications, magnetic zeolite–palladium–nickel ferrite is a suitable catalyst for the Suzuki–Miyaura cross-coupling reaction. This catalyst has the advantage of high yield, easy reusability, and short reaction time [16].

Small-sized nanoparticles are widely used in applications such as hydrogen storage, catalysis, and nanoelectronics. The high stability of nickel nanoparticles was found to have high hydrogen storage capacity [17]. Nickel-doped nanocomposite with hollow nanoparticles when used as an anode shows enhanced electrical conductivity and large pseudocapacitive effect, leading to fast kinetics. Nickel-doped cobalt–sulfur nanocomposite exhibits excellent sodium storage when used as an anode [18]. Cellulose-coated nickel–chitosan composite filter paper was used as a dip catalyst for the conversion of toxic compounds. The nanocomposite displayed excellent activity and reusability in the degradation of 4-nitrophenol and 2-nitrophenol and reduction of methyl orange dye [19]. The metallization of textile with NiNPs greatly enhanced its electrical properties when used in smart textile and wearable electronics. NiNPs on the surface of fabric serve as conducting textile as well as electromagnetic shielding material [20].

A variety of techniques for the synthesis of NiNPs were reported in our recent work such as top-down synthesis routes including laser ablation, mechanical milling, nanolithography, thermal decomposition, and sputtering. Similarly, reported are bottom-up techniques essentially involving coprecipitation, sol–gel techniques, and plant-mediated synthesis [21]. These techniques are often associated with challenges and impediments. Several such techniques are critically discussed as follows: First, the synthesis of NiNPs *via* the solvothermal oleylamine route requires standard air-free procedures coupled with space and time-consuming experimental setup [22]. Second, traditional wet methods require several stages in the synthetic protocol. This technique was employed in the synthesis of metastable superparamagnetic hexagonal-packed NiNPs in different ionic liquids. The soft, wet-chemical synthesis produced the nickel hexagonal close-packed (hcp) phase, rather than the stable nickel face-centered cubic (fcc) phase after several stages as reported by Wegner *et al.* [23]. Third, in the hydrothermal synthesis of NiNPs, highly reactive and flammable sodium phosphide, sodium hypophosphite, and red phosphorus have often been used, making the synthesis potentially explosive [24]. These problems and drawbacks have been minimized by the application of a one-pot synthetic route in the current project.

The one-pot synthetic approach is simple and rapid in comparison to traditional wet-chemical methods, which require long synthetic regimes [23]. Wet chemical methods are costly, involving the use of metal catalyst and toxic precursors such as nickel carbonyl and sodium hypophosphite [25]. This includes sol–gel techniques in which the products are associated with high carbon content [26]. Although solvothermal methods have the combined challenges of technical processability and economic feasibility [27], the introduction of one-pot synthesis to obtain monodispersed nanoparticles with the mean size and the narrow average size distribution remains a challenge in applications of NiNPs [28]. Unprotected NiNPs with large surface areas readily undergo oxidation; hence, conventional synthetic techniques of NiNPs are not suitable options [21]. The synthesis of NiNPs stabilized in polyethylene glycol (PEG) is a promising solution to overcome the instability of NiNPs [29]. It is evident from the literature search that the modifier materials in this study have not been employed for NiNPs synthesis elsewhere. Moreover, nontoxic precursor and modifier materials were employed in the synthesis. Consequently, the selected materials are compatible with green chemistry.

In this study, we successfully synthesized NiNPs, protected by PEG. The one-pot solvothermal technique was employed with the aid of environmentally friendly chemicals. A systematic investigation of the reaction parameters, namely, effects of reaction temperature, pH of the precursor solution, the concentration of reactants, and reaction time on the formation of NiNPs, was carried out to obtain the optimal values for the synthesis. The optimum reaction temperature, pH, $NiCl_2{\cdot}6H_2O$ concentration, and reaction time are 190°C, pH 9, 0.1 M, and 24 h, respectively. The as-synthesized NiNPs were effectively characterized. Furthermore, to address the challenges and disadvantages associated with synthesis techniques, a simple, rapid, and moderately low-temperature procedure was employed. Crystalline nanoparticles were obtained using a cost-effective precursor, stabilizing agent, and capping agent. The NiNPs were directly fabricated by heating the mixture of nickel chloride, sodium acetate (NaAc), and PEG in ethylene glycol (EG) as the solvent under solvothermal conditions.

2 Experimental

2.1 Materials

Nickel chloride hexahydrate ($NiCl_2{\cdot}6H_2O$) (purity, 98.5%) and PEG $(HOCH_2CH_2OH)_n$ (M_w = 10,000) were purchased from Sigma-Aldrich (M) Sdn Bhd. EG ($HOCH_2CH_2OH$) (99.5%), sodium acetate (CH_3COONa) (NaAc) (purity, 99.5%), and ethanol (CH_3CH_2OH) (99.9%) were purchased from QReC (M) Sdn Bhd. Ammonium hydroxide (NH_4OH) (25%) was supplied by Merck Darmstadt, Germany. All chemicals in this study were of analytical grade, and no further purification was required.

2.2 Synthesis of nickel nanoparticles

The synthesis of NiNPs was carried out by a one-pot solvothermal route. In a typical procedure, 50 mL of 0.1 M of $NiCl_2{\cdot}6H_2O$ was added to 160 mL of EG, followed by 18 g of NaAc in a 500 mL three-neck flask to form a colloidal solution under vigorous stirring at room temperature for 60 min until a homogenous light green solution was obtained. Thereafter, 2.5 g of PEG (M_w = 10,000) was added to the mixture, followed by another intensive stirring for 2 h at 60°C. The pH of the mixture was adjusted to 9 with the help of 25% NH_4OH. Subsequently, the mixture was sealed in a Teflon-lined stainless-steel autoclave. The autoclave was inserted into an oven and heated at 190°C for 24 h. The oven was cooled down naturally to room temperature. The solution obtained was centrifuged at 10,000 rpm for 10 min. Then, the black powder was washed three times with ethanol, followed by distilled water. The final products were dried in a vacuum oven at 90°C for 12 h. The flow chart for the synthesis is shown in Figure 1.

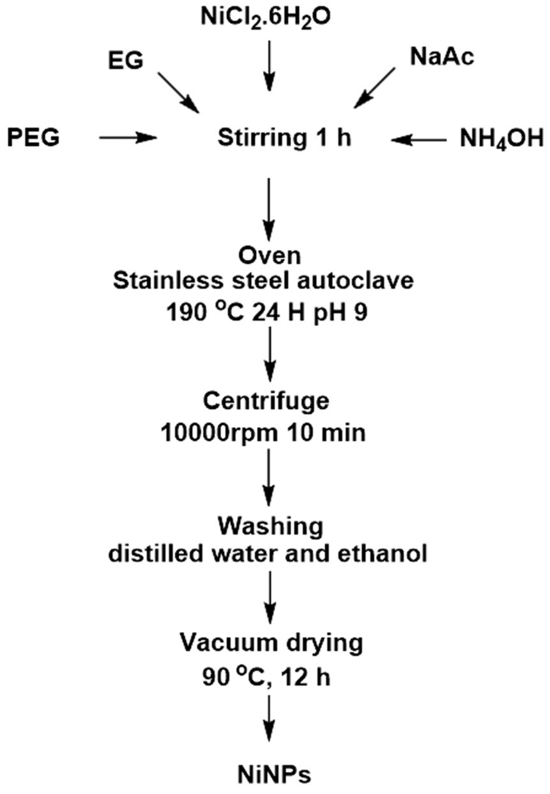

Figure 1: Flow chart of the one-pot solvothermal synthesis of NiNPs.

2.3 Characterizations

Ultraviolet-visible (UV-Vis) spectrophotometry was used to determine the characteristic maximum wavelength ($\lambda_{\max}$) surface plasmon resonance (SPR) of the bulk nickel chloride and NiNPs. The UV-Vis spectra were recorded on a Shimadzu (Model UV-2600) spectrophotometer from 200 to 800 nm. Fourier transform infrared spectra (FT-IR) was recorded on PerkinElmer spotlight (ATR-FTIR) 2000 FT-NIR spectrometer operating in a diffuse reflectance mode. Samples were exposed to 32 scans, and the spectra were acquired at a resolution of 4 cm^{-1} in the range of 4,000–600 cm^{-1}. X-ray powder diffraction (XRD) was used to determine the structure and phase composition of the synthesized NiNPs using the advanced X-ray diffractometer (Germany) with Cu Kα ($\lambda = 1.54178$ Å) X-ray radiation source and a sodium iodide scintillation type detector at $\leq$10°C $\geq$ 80°C. The average particle size of the NiNPs was estimated in accordance with the Scherrer equation. Transmission electron microscopy (TEM) images of the NiNPs were acquired using model Philips CM 12 with DOCU version 3.280 kV TEM. The sample preparation was carried out by dispersing a drop of the synthesized NiNPs suspension after 15 min sonication onto a Cu grid stabilized in carbon and maintained at room temperature. After 5 min, the Cu grid was washed with ethanol to remove PEG and allowed to dry for 10 min. Selected areas of the grid were subjected to the TEM analysis. Thermogravimetric analysis (TGA) was carried out to determine the material decomposition and thermal stability through mass change as a function of temperature. It was performed using an STA 6000 Thermogravimetric Analyser (Perkin Elmer). The samples were tested under an N_2 gas flow with a heating rate of 20°C min^{-1} in the temperature range of 30–800°C.

3 Results and discussion

3.1 Effect of reaction parameters

Optimization in chemical reactions is the process that seeks to solve the problems of minimizing or maximizing the values of the chosen reaction parameters. It serves as a strategy for improving the efficiency of a parameter by observing how the system responds to changes when a parameter's level is increased or decreased. Optimization techniques are implemented to find the best parameter combination or optimal values of a parameter property [30]. The effect of four synthesis influencing reaction parameters, namely, reaction temperature, pH of reactants, the concentration of the reactants, and time of reaction, was investigated with the aid of UV-Vis spectroscopy to obtain the specific value of a parameter that yielded the optimal results for the formation of NiNPs in the one-pot solvothermal synthesis. The optimization is time consuming, and therefore, it is not economically viable. However, it is necessary to conduct optimization to determine reaction parameters' optimal values. The synthesis technology is relatively fast and economical.

3.1.1 Effect of reaction temperature on the formation of nickel nanoparticles

The effect of reaction temperature on the formation of NiNPs at 100, 150, and 190°C was investigated at a reactant concentration of 0.1 M, pH 9, and reaction time of 24 h. The UV-Vis spectra are shown in Figure 2.

At 100°C, the absorbance maximum ($\lambda_{\max}$) for nickel chloride was at 394 nm and 265 nm for NiNPs. The band at 394 nm corresponds to the unreacted nickel chloride. While the band at 265 nm shows the formation of NiNPs. We suggest that nickel chloride did not dissociate entirely into its component ions; hence, the peaks at 394 and 265 nm for nickel chloride and NiNPs, respectively. Increasing the temperature to 150°C leads to a NiNP peak that appears at 265 nm, indicating a significantly accelerated reduction of the precursor nickel chloride. In the case of further increase of the temperature to 190°C, the nickel chloride peak disappears, and NiNP peak appears. We postulate that a higher frequency of ions with effective collisions in the solution leads to more products with a consequent increase in the intensity of the absorbance peak in agreement with the intensities reported by Xu *et al.* [31].

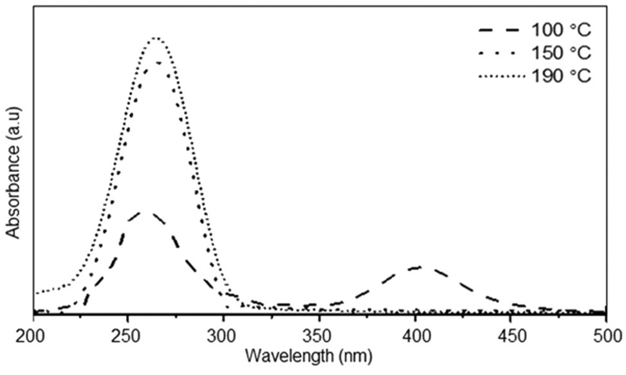

Figure 2: UV-Vis spectra of NiNPs at 100, 150, and 190°C.

3.1.2 Effect of reaction pH on the formation of nickel nanoparticles

The effect of pH on the formation of NiNPs was investigated at pH 9, 10, and 11. The following reaction parameters were kept constant, *i.e.*, temperature at 190°C, the concentration of precursor of 0.1 M, and reaction time at 24 h. The UV-Vis spectra obtained at these conditions are shown in Figure 3.

At pH 9, a single peak was centered at 265 nm for the formation of NiNPs. When the pH was increased to 10, the SPR of absorbance maximum was detected at 208 nm. However, at pH 11, the absorbance maximum shifted to 204 nm. There is a blue shift from 265 nm through 208–204 nm as the pH was increased from 9 to 11. Habte *et al.* [32] noted a similar blue shift and concluded that the blue shift might be due to the quantum confinement effect. Similarly, Abdullah *et al.* [33] reported that as the pH increases from 8 to 9, the absorption peak shifts slightly to a shorter wavelength (blue shift) ascribed to the formation of smaller nanoparticles. Nouri *et al.* [34] noted that the slight blue shift in the SPR band peak could be attributed to the formation of nanoparticles with smaller size and increased monodispersity. Alqadi *et al.* [35] have also reported that the increase in the pH will result in the wavelength shifting to shorter wavelengths because of a decrease in the size of the nanoparticles. Therefore, the shift in the SPR band peak from 265 to 204 nm is attributed to the formation of small-sized NiNPs.

3.1.3 Effect of reactant concentration on the formation of nickel nanoparticles

The effect of $NiCl_2\cdot6H_2O$ concentration as a reactant on the formation of NiNPs was investigated at 0.01, 0.05, and 0.1 M. The parameters kept constant were temperature at 190°C, pH 9, and reaction time at 24 h. The results obtained are presented in Figure 4.

At a low concentration, no significant peak appeared in the UV-Vis spectrum due to the little precursor quantity needed to start the nucleation of NiNPs. When the concentration was increased to 0.05 M, the peak at 265 nm appeared, and at 0.1 M, the peak became significant. When the precursor concentration increased, a greater number of nuclei will form due to an increase in the reaction rate as more Ni^{2+} nuclei are formed. The peak at a wavelength of 265 nm signifies the formation of NiNPs for the solvothermal synthesis. The intensity of absorbance peaks increased with an increase in the reactants' concentration due to the formation of more NiNPs [36].

3.1.4 Effect of reaction time on the formation of nickel nanoparticles

The effect of reaction time on the solvothermal synthesis of NiNPs was investigated at various reaction times of 10, 16, and 24 h while maintaining a constant reaction temperature of 190°C and pH 9. The results obtained with UV-Vis spectroscopy are shown in Figure 5.

The UV-Vis spectra clearly show that at a reaction time of 10 h, products were not formed because only a single peak corresponds to the SPR of nickel chloride. Observation of the UV-Vis spectrum at 16 h show two peaks centered at 394 and 265 nm. Therefore, at 16 h, some reactants were converted to products. However, at 24 h, only the peak at 265 nm was observed as all the reactants were converted to products, *i.e.*, NiNPs. Hence, a longer reaction time of 24 h favors the formation of

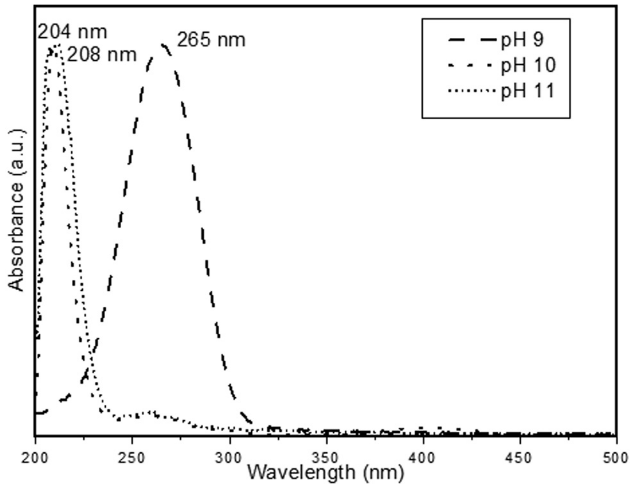

Figure 3: UV-Vis spectra of NiNPs at pH 9, 10, and 11.

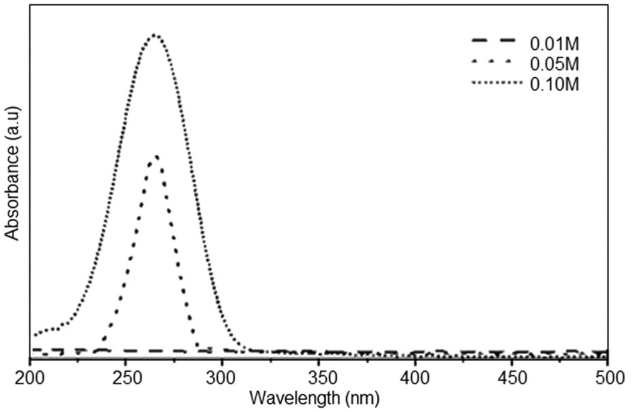

Figure 4: UV-Vis spectra of NiNPs at 0.01, 0.05, and 0.1 M.

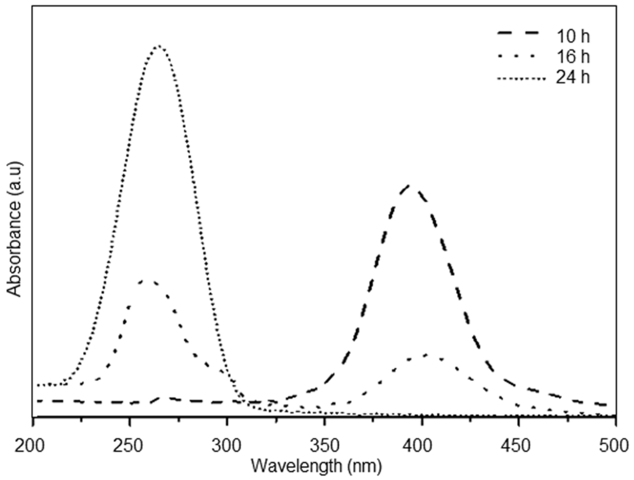

Figure 5: UV-Vis spectra of NiNPs at a reaction time of 10, 16, and 24 h.

PEG-protected NiNPs as shown by the UV-Vis analysis similarly reported by Magalhães Sousa *et al.* [37].

3.2 The UV-visible spectroscopy of nickel chloride and nickel nanoparticles

The wavelength of the SPR was recorded to verify the absorbance maximum ($\lambda_{\max}$) ($NiCl_2{\cdot}6H_2O$ and NiNPs) and to determine the size of the nanoparticles, shape, and the spectral width of the SPR of the nanoparticles (Figure 6).

The UV-Vis showed that the absorption band $\lambda_{\max}$ 394 of $NiCl_2{\cdot}6H_2O$ shifted to $\lambda_{\max}$ 265 is attributed to NiNPs SPR. The significant peak observed at $\lambda_{\max}$ 265 for NiNPs is due to the successful reduction of $NiCl_2{\cdot}6H_2O$ to NiNPs as the completion of reduction and was observed by the change in color of the reaction mixture from green to black. Although SPR of NiNPs was observed at $\lambda_{\max}$ 265 nm in our one-pot solvothermal process, the result is still considered as a characteristic of NiNPs as Elango *et al.* [38] reported $\lambda_{\max}$ at 252 nm, while Kumar *et al.* [39] recorded the $\lambda_{\max}$ of NiNPs at 309–343 nm.

The blue shift in the SPR from $\lambda_{\max}$ 394 to $\lambda_{\max}$ 265 nm, indicating that the size of the NiNPs, has become smaller. There is a blue shift as the pH was increased from 9 to 11 due to a decrease in the size of NiNPs [40]. The results also indicate that the NiNPs are monodispersed in size distribution due to the symmetrical shape of the SPR.

3.3 The FT-IR analysis of raw materials and product

FT-IR spectroscopy was used to study the functional groups present on the raw materials, namely, EG, PEG, $NiCl_2$, and the product NiNPs. The FT-IR of the raw materials and products are summarized in Figure 7.

The FT-IR analysis confirmed the presence of EG with prominent peaks at 3,286 cm^{-1} corresponding to O–H stretching, 2,870 cm^{-1} corresponding to H–CH bond vibration, and 1,031 cm^{-1} corresponding to C–O bond vibration. The presence of PEG was confirmed by FT-IR peaks at 2,836, 1,468, and 1,093 cm^{-1} corresponding to CH_2 bond,

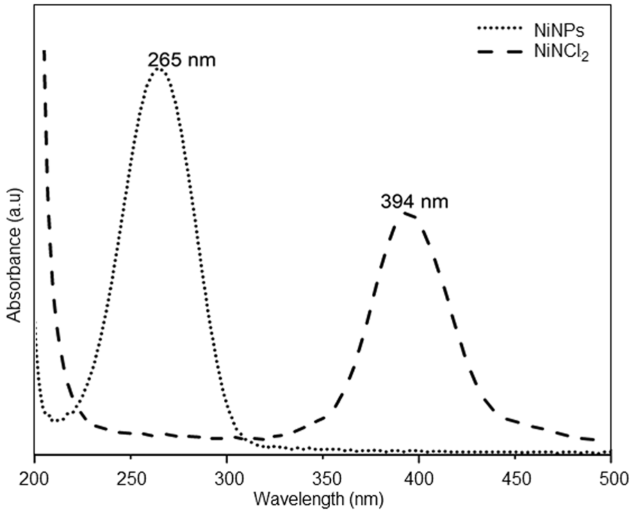

Figure 6: Overlay of the $\lambda_{\max}$ SPR of NiNPs and bulk nickel solution.

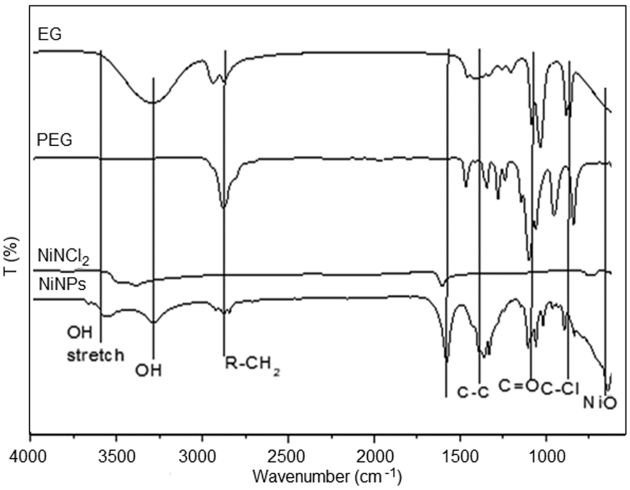

Figure 7: FT-IR spectra of EG, PEG, $NiCl_2$, and NiNPs.

C–C group, and C–O stretching, respectively [41]. In the FT-IR spectrum of aqueous nickel chloride, there are characteristic absorption bands at 3,388, 1,595, and 732 cm^{-1} corresponding to O–H stretch from water due to its interaction with nickel, 1,595 cm^{-1} is due to the interaction of NiO + H_2O, and 732 cm^{-1} is the band of inorganic material $NiCl_2$. In the spectrum of NiNPs, the characteristic absorption peak observed at 3,593 cm^{-1} is assigned to the adsorbed moisture by PEG with stretching vibration of the surface hydroxyl group that corresponds to O–H stretch from Ni $(OH)_2$ [42]. The band at 2,866 cm^{-1} is for CH_2, while that at 1,395 cm^{-1} is for C–C bond and 1,024 cm^{-1} is for C–O bond. The band at 850 cm^{-1} corresponds to C–Cl bond and that at 630 cm^{-1} corresponds to the Ni–O stretching mode. For most of the oxides, absorption bands are in the low wavenumber fingerprint region, and hence, the bands that occurred at 678, 624, and 552 cm^{-1} are assigned to the bonding between Ni and O. The Ni–O phase formation, which is a broad absorption band in the region of 820–400 cm^{-1}, is assigned to Ni–O stretching vibration mode [43]. Similarly, Gao *et al.* [42] noted that a peak observed at 565 cm^{-1} is due to the presence of the Ni–O stretching mode.

The formation of –COOH was predicted from the band at 1,387 cm^{-1}, corresponding to the –O–C–O stretching vibration. Electrolytic oxidation studies of EG on nickel in the presence of alkaline medium were reported to show higher oxides such as NiOOH from $Ni(OH)_2$ [44]. The sharp band at 894 cm^{-1} also confirms the oxidation of EG to form $CO_3{}^{2-}$. The principal function of the capping agent, PEG, is its ability to form functional groups on the NiNPs surface, thereupon restricting the particle size and improving the particle stability. The pure NiNPs spectrum revealed the presence of O–H bond stretching in the range of 3,000–3,500 cm^{-1}. Similarly, the peaks at 1,052 and 1,027 cm^{-1} correspond to the EG functional groups. These functional groups might influence the particle size. NiNPs protected by such a robust capping agent is not an active catalyst, and high-temperature treatments used to activate NiNP catalyst often cause inevitable aggregation and catalytic deterioration of the nanoparticles, similar to that reported by Ádám *et al.* [45].

The presence of EG and PEG peaks in the FT-IR spectrum of NiNPs confirms their use as a solvent and a capping agent, respectively. The synthesized NiNPs were washed with ethanol to remove functional groups on the surface of the NiNPs. However, removing the functional groups from particle surfaces leads to NiNP agglomeration *via* strong magnetic forces. The presence of Ni–$(OH)_2$ and NiO in the FT-IR spectra indirectly indicates the synthesis of NiNPs [46].

3.4 The XRD analysis of nickel nanoparticles and nickel chloride

The XRD pattern was employed to characterize the structural features, crystalline information, and phase purity of the precursor $NiCl_2{\cdot}6H_2O$ (Figure 8a) and the synthesized NiNPs (Figure 8b). The results match well with the standard cards of pure $NiCl_2{\cdot}6H_2O$ JCPDS card (No. 025-10440) and pure powder NiNPs of JCPDS card (No. 04-0850) [23].

Four characteristic diffraction peaks for pure nickel were observed at 33.50°, 44.50°, 52.10°, and 76.40°. These peaks correspond to the four indexed planes (100), (111), (200), and (220), respectively. The XRD results show significantly pure NiNPs. The results showed that pure nickel in the face-centered cubic structure was produced without oxidation. There are no peaks showing the incomplete reduction of the precursor, nickel chloride. The size of the crystallite was estimated from the most intense peak (111) of the XRD diffraction pattern using the Scherrer formula [47]. As the crystallite size decreased, the full width at half maximum (FWHM) increased, and the reflection intensities change accordingly. The crystallite size calculated from the most intense peak has a value of 24 nm, and this confirmed the primary NiNPs. The two results were compared to conclude the successful synthesis of NiNPs.

3.5 TEM of nickel nanoparticles

TEM analysis is one of the most powerful methods to acquire the three-dimensional atomic arrangement

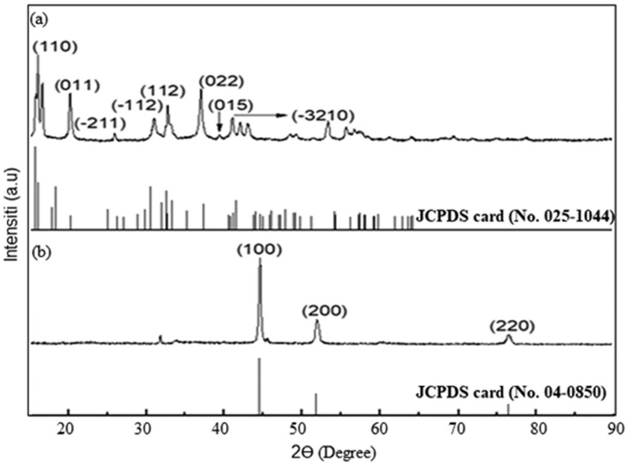

Figure 8: (a): XRD pattern of $NiCl_2{\cdot}6H_2O$ with the standard card (b): XRD pattern of NiNPs with the standard card.

directly. By taking electron diffraction patterns along several crystal directions, fundamental structural information such as lattice constants and crystal systems can be obtained [48]. The particle size of the synthesized NiNPs was analyzed by TEM, as shown in Figure 9(a). The bright field and dark field images indicate that the samples have a large polymer region surrounding the NiNPs. The dark field images suggest the presence of crystalline NiNPs. The images reveal that the NiNPs are solid, spherical, and agglomerated. Large spherical nanoparticles of pure Ni are composed of smaller crystalline NiNPs. Small particles tend to aggregate into large nanoparticles through van der Waals attraction during thermal decomposition, as reported by Wu *et al.* [49].

The smaller crystalline NiNPs begin to aggregate in the initial stages of the growth mechanism, leading to the generation of large aggregates. The driving force for this oriented aggregation is obtained from the minimization of interfacial energy [50]. The morphology of NiNPs is adequately modulated by the introduction of stabilizing and capping agents into the reaction medium. Hence, the selective interaction of the stabilizing and capping agents on the facet of the first-formed NiNPs determines the nanoparticles' growth [21]. However, the stability of the NiNPs was achieved by the presence of the capping agent PEG, which binds to the surface of the nanoparticles to prevent their aggregation. Due to the high kinetics of the reaction, the occurrence of structural defects, such as twins, during the nucleation and growth steps, producing singly or multiply twinned nuclei is very common [51].

The polycrystalline structures were achievable due to the lengthy polymer chain in the capping agent PEG, predominantly leading to agglomeration of the NiNPs. Moreover, to decrease the high surface energy, the NiNPs preferentially agglomerate during their formation in the liquid phase. Conversely, Ni nuclei gathered the adjacent magnetic dipole–dipole interaction with van der Waals forces *via* self-assembly in a common crystallographic orientation and joined the smaller nanoparticles at a planar interface [52]. Hence, the magnetic properties of NiNPs account for the agglomeration observed.

The particle size distribution of NiNPs from the histogram gave an average diameter of 49.2 ±1.3 nm. The mean diameter of relatively small particles was 40.0 ±1.3 nm, and the mean particle diameter of large particles was 70.0 ±1.3 nm. The mechanism that affects the average size and size distribution during the reaction has not been completely understood. It could be that Ostwald ripening takes place, where small particles are consumed by the larger particles. In comparison, the particle size derived from the TEM histogram (49 nm) is larger than the particle size calculated from the XRD pattern using the Scherrer equation with a value of 24 nm. The larger TEM particle size distribution was attributed to agglomeration, the inhomogeneity in size, shape, composition, and crystallinity of the sample. While the results obtained by the Scherrer equation are strongly dependent on the geometry of the nanoparticles as well as sensitivity to the crystallite domain on each particle and subsequently by the lattice defects. Therefore, the particle size calculated by the Scherrer equation is smaller than the particle size determined from the TEM-generated histogram. Moreover, the difference in scattering due to the amorphous capping agent PEG on the surface layer of the NiNPs dramatically affects the results derived from the Scherrer equation in agreement with Neiva *et al.* [51].

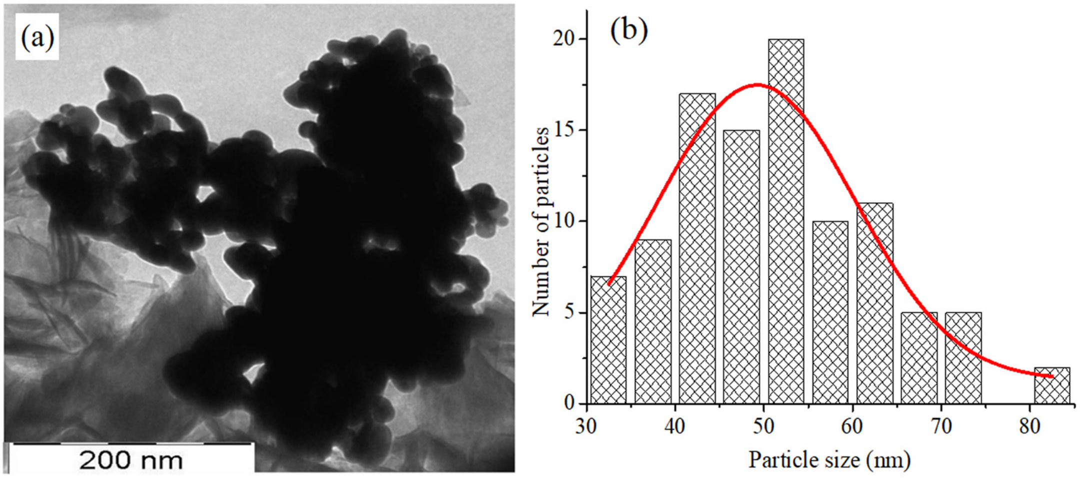

Figure 9: (a) TEM image of NiNPs at mag. 200 nm. (b) Diameter distribution of 100 particles NiNPs using Image-J.

3.6 Thermal characterization of nickel nanoparticles

TGA [53] was conducted to determine the thermal decomposition temperature and the heat resistance of the synthesized NiNPs in N_2 atmosphere and compared to its precursor, $NiCl_2{\cdot}6H_2O$ (Figure 10).

The characteristics of $NiCl_2{\cdot}6H_2O$ are indicated by the major two stages of decomposition temperature. The first stage of decomposition (T_1) started at 100°C and came to an end at 300°C, indicating the moisture removal of hexahydrate molecules of $NiCl_2{\cdot}6H_2O$, and the second stage of decomposition (T_2) occurred at >650°C, indicating the breaking of the Ni–Cl bond. There was more than 55% of residue once the degradation was completed at 800°C due to the contribution of Ni constituents of $NiCl_2{\cdot}6H_2O$.

As the $NiCl_2{\cdot}6H_2O$ converted to NiNPs, the characteristic of $NiCl_2{\cdot}6H_2O$ thermogram significantly disappeared, thus proving that NiNPs were successfully synthesized through the solvothermal process. Once the degradation was completed at 800°C, more than 97% of residues are shown. These occurrences may be due to the removal of moisture typically trapped inside NiNP particles or the decomposition of the thin PEG coating around the NiNPs or the removal of water molecules, which were attached to PEG coating. Wang *et al.* [54] studied the effect of cross cold rolling and annealing on microstructure and texture in pure nickel. They obtained results comparable to this TGA results in the annealing of commercially available pure nickel at 550°C. The TGA results agree with the decomposition of NiNPs reported by Bathla and Pal [44] and De Jesús *et al.* [55].

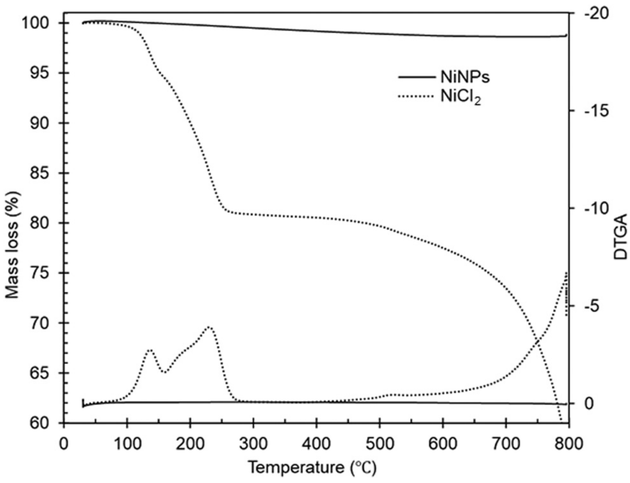

Figure 10: TGA and DTGA of NiNPs and $NiCl_2{\cdot}6H_2O$.

3.7 Summary of the synthesis and proposed reaction mechanism

A one-pot solvothermal dissociation of nickel chloride occurs in oxygen-free, high boiling EG. The polarity of the mixture acts as a reducing agent in the stainless-steel autoclave at 190°C, leading to the formation of NiNPs. Inorganic microstructures undergo fast nucleation and growth in an aqueous medium with high temperature and pressure. In the oven, NiNPs undergo rapid nucleation and growth due to the high temperature and high pressure in the stainless-steel autoclave. The application of PEG promotes the controlled surfactant-assisted reaction, leading to a stepwise growth mechanism of the NiNPs as a response, which was similarly reported by Jaji *et al.* [21].

The NiNP formation process can be deduced from the chemical reaction leading to the reduction of nickel ions to NiNPs and is formulated based on the following processes: first, the high temperature and high pressure attainable in the stainless-steel autoclave during the reaction enable the precursor $NiCl_2{\cdot}6H_2O$ to dissociate into its component ions. The initial process involves Ni^{2+} cation generation. Second, the solvent EG undergoes oxidation under such conditions to yield nickel ions. Finally, nickel ions are reduced to NiNPs in the liquid polyol phase by duplicative oxidation of acetaldehyde, produced by the dehydration of EG.

$$NiCl_2 \cdot 6H_2O \rightarrow Ni^{2+} + 2Cl^- + 6H^+ + 6OH^-. \tag{1}$$

Then, the solvent EG undergoes oxidation under such conditions to yield the following:

$$HOCH_2CH_2OH \rightarrow CH_3CHO^- + H_2O. \tag{2}$$

Finally, nickel ions are reduced to NiNPs in the liquid polyol phase by duplicative oxidation of acetaldehyde, produced by the dehydration of EG.

$$2CH_3CHO^- + Ni^{2+} \rightarrow CH_3COCOCH_3 + H_2O + Ni. \tag{3}$$

The mechanism of the reaction may be formulated from equations (1)–(3), taking into consideration the stabilizing agent NaAc as well as the capping agent PEG, as shown in Figure 11. In line with the Ostwald ripening mechanism, free Ni^{2+} cations are nucleated in the solvent [56]. The NiNPs are surrounded by the stabilizing agent NaAc.

The Ni^{2+} cations react with the stabilizing agent sodium acetate to form a comparatively stable intermediate of Ni^{2+}. Meanwhile, sodium acetate was used as an electrostatic stabilizing agent to prevent nickel cations from agglomeration. Hydrated sodium acetate

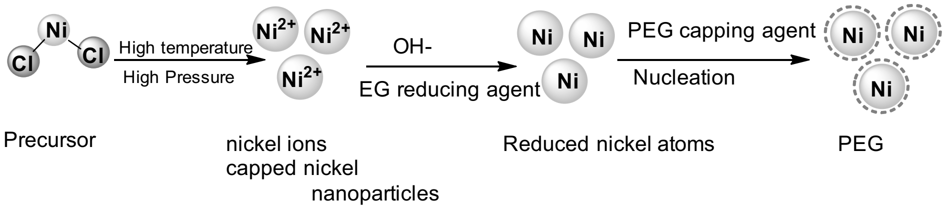

Figure 11: Schematic representation of the solvothermal reaction mechanism.

plays a significant role in the formation of Ni^{2+} complexes as metal precursors. The nickel complexes decompose and release free Ni^{2+} ions to form nanocrystalline Ni by its chemical reaction with EG.

4 Conclusions

A simple, one-pot solvothermal synthesis of self-protected NiNPs was successfully carried out. In this method, nickel chloride was used as the precursor, EG as the solvent, sodium acetate as the stabilizing agent, and PEG as the capping agent. A systematic investigation of the reaction parameters, namely, effects of reaction temperature, pH of precursor solution, the concentration of reactants, and reaction time on the formation of NiNPs, was carried out to obtain the optimal values for the synthesis. The optimum reaction temperature, pH, $NiCl_2{\cdot}6H_2O$ concentration, and reaction time are 190°C, pH 9, 0.1 M, and 24 h. The FT-IR results indicate the presence of –OH stretching band at 3,593 cm^{-1} due to its interaction with Ni and NiO at 603 cm^{-1}, which are absent in the FT-IR spectrum of nickel chloride solution, EG, and PEG, indicating that NiNPs have been synthesized. The UV-Vis analysis reveals a shift in the SPR of the aqueous nickel solution from λ_{max} 394 nm to λ_{max} 265 nm in the NiNPs, indicating a blue shift. The XRD analysis confirms the presence of the FCC phase with the calculated particle size of 24 nm. However, the TEM image shows the mean particle diameter (49 nm) of the nickel nanoparticle. TGA showed that the degradation of NiNPs was completed at 800°C with more than 97% residue. Hence, the synthesized NiNPs can be used as fillers to enhance thermal, mechanical, and electrical properties of high-performance polyamides. However, PEG-protected NiNPs are not active catalysts. Their activation by high-temperature treatments leads to nanoparticles aggregation as well as catalyst deterioration. The optimization is time consuming, and therefore, it is not economically viable. However, it is necessary to conduct optimization to determine optimal values of reaction parameters. The synthesis technology is relatively fast, economical, and in line with green chemistry. Further studies are recommended to address these challenges.

Acknowledgments: The authors would like to thank the School of Chemical Sciences, Universiti Sains Malaysia for technical support.

Funding information: The authors wish to acknowledge Universiti Sains Malaysia for sponsoring this project under short term grant USM-STG-6315076 and Individual Research University Grant (1001/P Kimia/8011086). Nuru-Deen Jaji wishes to thank the Federal College of Education Technical Gombe, Nigeria, for TETFUND Postgraduate Scholarship.

Author contributions: Muhammad Bisyrul Hafi Othman and Hooi Ling Lee: conceptualization. Nuru-Deen Jaji: formal analysis and investigation. Muhammad Bisyrul Hafi Othman and Hooi Ling Lee: resources. Nuru-Deen Jaji: data curation, writing, and original draft preparation. Muhammad Bisyrul Hafi Othman, David Hui, Hooi Ling Lee, and Mohd Hazwan Hussin: validation, editing, visualization, and supervision. Muhammad Bisyrul Hafi Othman and David Hui: project administration. All authors have accepted responsibility for the entire content of this manuscript and approved its submission.

Conflict of interest: David Hui, who is the co-author of this article, is a current Editorial Board member of *Nanotechnology Reviews*. This fact did not affect the peer-review process. The authors declare no other conflict of interest.

References

[1] Zhan J, Yao X, Zhang X. Shock response of metal-ceramic nanolayered composites. Compos B Eng. 2020;199:108272.
[2] Wu Q, Miao WS, Zhang YD, Gao HJ, Hui D. Mechanical properties of nanomaterials: a review. Nanotechnol Rev. 2020;9(1):259–73.
[3] Yao Y, Lan L, Liu X, Ying Y, Ping J. Spontaneous growth and regulation of noble metal nanoparticles on flexible biomimetic

MXene paper for bioelectronics. Biosens Bioelectron. 2020;148:111799–806.

[4] Tomitaka A, Takemura Y, Huang Z, Roy U, Nair M. Magnetoliposomes in controlled-release drug delivery systems. Crit Rev Biomed Eng. 2019;47(6):495–505.

[5] Kishimoto F, Matsuhisa M, Imai T, Mochizuki D, Tsubaki S, Maitani MM, et al. Remote control of electron transfer reaction by microwave irradiation: kinetic demonstration of reduction of bipyridine derivatives on surface of nickel particle. J Phys Chem Lett. 2019;10(12):3390–4.

[6] Liu C, He X, Deng X, Wu Y, Zheng Z, Liu J, et al. Application of nanomaterials in ultra-high performance concrete: a review. Nanotechnol Rev. 2020;9(1):1427–44.

[7] Li H, Yang S, Hui D, Hong R. Progress in magnetic Fe3O4 nanomaterials in magnetic resonance imaging. Nanotechnol Rev. 2020;9(1):1265–83.

[8] Darwish AM, Sarkisov SS, Wilson S, Wilson J, Collins E, Patel DN, et al. Polymer nanocomposite sunlight spectrum down-converters made by open-air PLD. Nanotechnol Rev. 2020;9(1):1044–58.

[9] Hao H, Hui D, Lau D. Material advancement in technological development for the 5G wireless communications. Nanotechnol Rev. 2020;9(1):683–99.

[10] Luo L, Zhou Y, Xu X, Shi W, Hu J, Li G. Progress in construction of bio-inspired physico-antimicrobial surfaces. Nanotechnol Rev. 2020;9(1):1562–75.

[11] Cheng Y, Guo M, Zhai M, Yu Y, Hu J. Nickel nanoparticles anchored onto Ni foam for supercapacitors with high specific capacitance. J Nanosci Nanotechnol. 2020;20(4):2402–7.

[12] Yang D, Gao L, Yang JH. New insights into layered graphene materials as substrates to regulate synthesis of Ni–P nanomaterials for electrocatalytic oxidation of methanol and water. ACS Appl Mater Interfaces. 2019;11(48):45189–98.

[13] Pan Y, Xu K, Wu C. Recent progress in supercapacitors based on the advanced carbon electrodes. Nanotechnol Rev. 2019;8(1):299–314.

[14] Yadav S, Hassan MS, Verma P, Sapra S. Nickel selenide nanoparticles as a cheap alternative for Pt-counter electrode in dye-sensitized solar cells. J Nanosci Nanotechnol. 2019;19(1):375–82.

[15] Döpke C, Grothe T, Steblinski P, Klöcker M, Sabantina L, Kosmalska D, et al. Magnetic nanofiber mats for data storage and transfer. Nanomaterials. 2019;9(1):92–103.

[16] Dehghani M, Tadjarodi A, Chamani S. Synthesis and characterization of magnetic zeolite Y-palladium-nickel ferrite by ultrasonic irradiation and investigating its catalytic activity in Suzuki-Miyaura cross-coupling reactions. ACS Omega. 2019;4(6):10640–48.

[17] Fadlallah MM, Abdelrahman AG, Schwingenschlogl U, Maarouf AA. Graphene and graphene nanomesh supported nickel clusters: electronic, magnetic, and hydrogen storage properties. Nanotechnology. 2019;30(8):085709–25.

[18] Zhou H, Cao Y, Ma Z, Li S. Facile synthesis of nickel-doped Co9S8 hollow nanoparticles with large surface-controlled pseudocapacitive and fast sodium storage. Nanotechnology. 2018;29(19):195201–08.

[19] Kamal T, Khan SB, Asiri AM. Nickel nanoparticles-chitosan composite coated cellulose filter paper: an efficient and easily recoverable dip-catalyst for pollutants degradation. Environ Pollut. 2016;218:625–33.

[20] Moazzenchi B, Montazer M. Click electroless plating of nickel nanoparticles on polyester fabric: electrical conductivity, magnetic and EMI shielding properties. Colloids Surf A Physicochem Eng Asp. 2019;571:110–24.

[21] Jaji ND, Lee HL, Hussin MH, Akil HM, Zakaria MR, Othman MBH. Advanced nickel nanoparticles technology: from synthesis to applications. Nanotechnol Rev. 2020;9(1):1456–80.

[22] Liu S, Qiao X, Liu W, Shi S, Qu Y. Mechanism of ultrasonic treatment under nickel salt solution and its effect on electroless nickel plating of carbon fibers. Ultrason Sonochem. 2019;52:493–504.

[23] Wegner S, Rutz C, Schütte K, Barthel J, Bushmelev A, Schmidt A, et al. Soft, wet-chemical synthesis of metastable superparamagnetic hexagonal close-packed nickel nanoparticles in different ionic liquids. Chem Eur J. 2017;23(26):6330–40.

[24] Ma ZC, Chen QD, Han B, Li HL, Wang L, Zhang YL, et al. Intense femtosecond laser-mediated electrical discharge enables preparation of amorphous nickel phosphide nanoparticles. Langmuir. 2018;34(20):5712–8.

[25] Eluri R, Paul B. Microwave assisted greener synthesis of nickel nanoparticles using sodium hypophosphite. Mater Lett. 2012;76:36–9.

[26] Muniandy SS, Kaus NHM, Jiang ZT, Altarawneh M, Lee HL. Green synthesis of mesoporous anatase TiO_2 nanoparticles and their photocatalytic activities. RSC Adv. 2017;7(76):48083–94.

[27] Imam SS, Adnan R, Kaus NHM, Hussin MH. Room-temperature synthesis of Bi/BiOBr composites for the catalytic degradation of ciprofloxacin using indoor fluorescent light illumination. J Mater Sci Mater Electron. 2019;30(6):6263–76.

[28] Heilmann M, Kulla H, Prinz C, Bienert R, Reinholz U, Guilherme Buzanich A, et al. Advances in nickel nanoparticle synthesis via Oleylamine route. Nanomaterials. 2020;10(4):713–25.

[29] Lin LK, Uzunoglu A, Stanciu LA. Aminolated and thiolated PEG-covered gold nanoparticles with high stability and antiaggregation for lateral flow detection of bisphenol A. Small. 2018;14(10):1702828–37.

[30] Alhijazi M, Zeeshan Q, Qin Z, Safaei B, Asmael M. Finite element analysis of natural fibers composites: a review. Nanotechnol Rev. 2020;9(1):853–75.

[31] Xu C, Nie D, Chen H, Wang Y, Liu Y. Template-free synthesis of magnetic CoNi nanoparticles via a solvothermal method. Mater Lett. 2015;138:158–61.

[32] Habte AG, Hone FG, Dejene FB. Effect of solution pH on structural, optical and morphological properties of SnO_2 nanoparticles. Physica B Condens Matter. 2020;580(2020):411832.

[33] Abdullah FH, Bakar NA, Bakar MA. Low temperature biosynthesis of crystalline zinc oxide nanoparticles from Musa acuminata peel extract for visible-light degradation of methylene blue. Optik. 2020;206(2020):164279.

[34] Nouri A, Yaraki MT, Lajevardi A, Rezaei Z, Ghorbanpour M, Tanzifi M. Ultrasonic-assisted green synthesis of silver nanoparticles using Mentha aquatica leaf extract for enhanced antibacterial properties and catalytic activity. Colloids Interface Sci Commun. 2020;35(2020):100252.

[35] Alqadi M, Noqtah OA, Alzoubi F, Alzouby J, Aljarrah K. pH effect on the aggregation of silver decrease in the size of the nanoparticles. Mater Sci. 2014;32(1):107–11.

[36] Badvi K, Javanbakht V. Enhanced photocatalytic degradation of dye contaminants with TiO_2 immobilized on ZSM-5 zeolite

modified with nickel nanoparticles. J Clean Prod. 2021;280(2021):124518.

[37] Magalhães Sousa D, Chiappim W, Leitão J, Lima JC, Ferreira I. Microwave synthesis of silver sulfide and silver nanoparticles: light and time influence. ACS omega. 2020;5(22):12877–81.

[38] Elango G, Roopan SM, Dhamodaran KI, Elumalai K, Al-Dhabi NA, Arasu MV. Spectroscopic investigation of biosynthesized Nickel nanoparticles and its larvicidal, pesticidal activities. J Photochem Photobiol B, Biol. 2016;162:162–7.

[39] Kumar P, Singh P, Kumar D, Prakash V, Hussain M, Das A. A novel application of micro-EDM process for the generation of nickel nanoparticles with different shapes. Mater Manuf Process. 2017;32(5):564–72.

[40] Kityk A, Shaiderov D, Vasil'eva E, Protsenko V, Danilov F. Choline chloride based ionic liquids containing nickel chloride: physicochemical properties and kinetics of Ni(ii) electroreduction. Electrochim Acta. 2017;245:133–45.

[41] Nematdoust S, Najjar R, Bresser D, Passerini S. Partially oxidized cellulose grafted with polyethylene glycol mono-methyl ether (m-PEG) as electrolyte material for lithium polymer battery. Carbohydr Polym. 2020;240:116339–48.

[42] Gao F, Tu X, Ma X, Xie Y, Zou J, Huang X, et al. NiO@Ni-MOF nanoarrays modified Ti mesh as ultrasensitive electrochemical sensing platform for luteolin detection. Talanta. 2020;215(2020):120891.

[43] Kaviyarasu K, Manikandan E, Kennedy J, Jayachandran M, Ladchumananandasiivam R, De Gomes UU, et al. Synthesis and characterization studies of NiO nanorods for enhancing solar cell efficiency using photon upconversion materials. Ceram Int. 2016;42(7):8385–94.

[44] Bathla A, Pal B. Catalytic selective hydrogenation and cross coupling reaction using polyvinylpyrrolidone-capped nickel nanoparticles. ChemistrySelect. 2018;3(17):4738–44.

[45] Ádám AA, Szabados M, Polyákovics Á, Musza K, Kónya Z, Kukovecz Á, et al. The synthesis and use of nano nickel catalysts. J Nanosci Nanotechnol. 2019;19(1):453–8.

[46] Li N, Li Y, Li Q, Zhao Y, Liu CS, Pang H. NiO nanoparticles decorated hexagonal nickel-based metal-organic framework: self-template synthesis and its application in electrochemical energy storage. J Colloid Interface Sci. 2020;581(Pt B):709–18.

[47] Sidorova EN, Dzidziguri EL, Vinichenko YP, Ozherelkov DY, Shinkaryov AS, Gromov AA, et al. Metal nanoparticles formation from nickel hydroxide. Mater. 2020;13(20):4689–702.

[48] Oku T. Crystal structures of perovskite halide compounds used for solar cells. Rev Adv Mater Sci. 2020;59(1):264–305.

[49] Wu MS, Chen FY, Lai YH, Sie YJ. Electrocatalytic oxidation of urea in alkaline solution using nickel/nickel oxide nanoparticles derived from nickel-organic framework. Electrochim Acta. 2017;258:167–74.

[50] Zhang H, Zhao Z, Turley AT, Wang L, McGonigal PR, Tu Y, et al. Aggregate science: from structures to properties. Adv Mater. 2020;32(36):2001457.

[51] Neiva EG, Bergamini MF, Oliveira MM, Marcolino Jr LH, Zarbin AJ. PVP-capped nickel nanoparticles: synthesis, characterization and utilization as a glycerol electrosensor. Sens Actuators B Chem. 2014;196:574–81.

[52] Kuznetsov AA. Zero-field and field-induced interactions between multicore magnetic nanoparticles (in Eng). Nanomaterials (Basel). 2019 May 9;9(5):718.

[53] Othman MBH, Akil HM, Osman H, Khan A, Ahmad Z. Synthesis, characterisation and thermal properties of hyperbranched polyimide derived from melamine via emulsion polymerisation. J Therm Anal Calorim. 2015;120(3):1785–98.

[54] Wang L, Chen X, Luo T, Ni H, Mei L, Ren P, Liu Q, et al. Effect of cross cold rolling and annealing on microstructure and texture in pure nickel. Rev Adv Mater Sci. 2020;59(1):252–63.

[55] De Jesús JC, García S, Dorante D. Size tunable carbon-encapsulated nickel nanoparticles synthesized by pyrolysis of nickel acetate tetrahydrate. J Anal Appl Pyrolysis. 2018;130:332–43.

[56] Wu ZG, Munoz M, Montero O. The synthesis of nickel nanoparticles by hydrazine reduction. Adv Powder Technol. 2010;21(2):165–8.